High resolution observations of friction-induced oxide and its interaction with the worn surface

RAINFORTH, W. M., LEONARD, A. J., PERRIN, C., BEDOLLA-JACUINDE, A., WANG, Y., JONES, H. and LUO, Quanshun <http://orcid.org/0000-0003-4102-2129>

High resolution observations of friction-induced oxide and its interaction with the worn surface

W.M. Rainforth*, A.J. Leonard, C. Perrin, A. Bedolla-Jacuinde, Y. Wang, H. Jones, Q. Luo

Department of Engineering Materials, The University of Sheffield, Mappin St., Sheffield, S1 3JD, UK

Abstract: A detailed transmission electron microscopy study of oxide and oxygen-containing phase formation during the sliding wear of metals, composites and coatings is provided. A wide range of different materials types are reported in order to compare and contrast their oxidational wear behaviour: a low carbon stainless steel, a H21 tool steel containing 7% TiC particles, a 17% Cr white iron, an Al-Si / 30%SiC composite, an Al-alloy (6092) – 15% Ni3Al composite and finally a 3rd generation TiAlN/CrN 'superhard' multilayer coating. For the ferrous alloys, nanoscale oxides and oxygen-containing phases were formed that exhibited excellent adhesion to the substrate. In all cases, an increase in oxide coverage of the surface was associated with a decrease in Lancaster wear coefficient. The oxide at the surface of the 316L and H21+7%TiC was found to deform with the substrate, forming a mechanically mixed layer that enhanced surface wear resistance. Evidence of oxidational wear is presented for the wear of the A-Si-30%SiCcomposite, but this did not give a beneficial effect in wear, a result of the brittle nature of the oxide that resulted in detachment of fine (150nm) thick fragments. The worn surface of the Al-alloy (6092)-15%Ni3Al and TiAlN/CrN coating was characterized by reaction with the counterface and subsequent oxidation, the product of which enhanced wear resistance. The observations are related to the classical theory of oxidational wear.

Keywords: Oxidational wear; Transmission electron microscopy; Nanostructures

1. Introduction

Since the first observation of oxidational wear by Fink [1], there has been much development of the theory. Most notably, Quinn and co-workers [2–17] have published a comprehensive theory for oxidational wear that is now the widely accepted basis for interpretation of worn surface morphology in the mild wear regime. The theory is reported to be broadly in agreement with experimental observations of oxidational wear (e.g.[18–22]).

The theories of Quinn are well developed and yield quantitative values for the most important variables(such as number of contacts (N), the real contact temperature at the asperities (T_c), activation energy (Q),Arrhenius constant for parabolic oxidation during wear (A_p), critical oxide thickness, ζ, etc). However, the theories assume a relatively simple structure of the surface oxide, namely that the oxide grows in a comparatively uniform manner at the contacting asperities, until a critical thickness, ζ, is reached, at which point spalling occurs (with detachment at the oxide/matrix interface)and the formation of wear debris. As a result, the asperity is no longer in contact, but it is replaced by a separate asperity, at which point the cycle is repeated. While this situation undoubtedly occurs (for example, as shown by SEM micrographs presented by Quinn [11]),there remains comparatively little detailed microstructural analysis to indicate how widely applicable this scenario is.

The majority of the work on oxidational wear focuses on ferrous alloys. It is clear that oxides play a major role in determining the wear rate of these materials, shown for example, by the classical work of Welsh [23]. However, little work has been undertaken to determine the extent to which oxidation is important in other metallic systems, for example, aluminium alloys, which have received much attention as tribological materials. Despite the substantial driving force for oxidation in this system, there is little report of oxidational wear in aluminium and its alloys.

In a comprehensive review of the subject [10,11], Quinn discussed the terminology used to classify wear and describe wear mechanisms, an area notorious for the plethora of descriptions and consequent lack of clear, widely accepted, definitions. In the current paper, the same approach will be taken as that of Quinn, namely the use of mild and severe wear; mild wear refers to the regime where the wear debris is dominated by reaction with the environment (and is therefore often an oxide)and is generally small (typically sub-micron), while severe wear is associated with extensive surface roughening and predominantly metallic wear debris, the dimensions of which are large in comparison to mild wear (typically two orders of magnitude greater than mild, i.e. 10–100 μm).However, the wear mechanism nomenclature used by Lim and Ashby [24] will also be used, since this allows the current test conditions and surface observations to be correlated with the wear maps proposed by these authors that cover a substantial proportion of the wear data. Moreover, Lim and Ashby fully referenced all the work of Quinn and others on mild and severe oxidational wear.

The current paper considers the detailed microstructural evolution at the worn surfaces of a range of materials that have substantially different characteristics and have been reported, at least in part, elsewhere [25–36]: ferrous alloys, aluminium based metal matrix composites and an advanced wear resistant coating. For the ferrous materials, a wide range of alloy types are considered, ranging from single phase (316L stainless steel)through to complex multiphase

Table 1 Compositions (weight%) of the alloys used in this investigation

Alloy description	C	Cu	Si	Cr	Ni	W	Mg	Fe	Other
Al–6092–Ni_3Al		0.90	0.73				0.99	0.06	15%Ni_3Al
Duralcan			7.58				0.47	0.08	30%SiC
316L	0.025		0.29	16.5	12.3			Bal	
17% Cr iron	2.56			16.8	1.77			Bal	1.93%Mo
H21+7%TiC	0.31		0.12	3.43		8.21		Bal	7%TiC, 0.37%V

structures containing high volume fractions of hard particles (tool steels with the addition of TiC, and white irons). Two aluminium alloy metal matrix composites are considered, one with a conventional SiC reinforcement, the other with a novel inter-metallic reinforcement (Ni3Al). Finally, a 'superhard' TiAlN/CrN multilayer wear resistant coating, with the potential to operate in high speed, unlubricated, cutting applications is also considered. Detailed transmission electron microscopy (TEM) has been used to understand the type and morphology of the oxide that forms and the manner in which it modifies surface structure. The similarities and differences between the behaviour of the oxides at the surface are discussed.

2. Experimental procedure

2.1. Materials

The compositions of the alloys used in the present study are given in Table 1. The AlSl 316L stainless steel(L denotes low carbon) was supplied as 15 mm round bar in the solution annealed and quenched condition from a local stockholder. The H21 tool steel with TiC additions up to 7vol% were obtained by vacuum melting commercial H21 feed stock and adding a FeWTiC master alloy (supplied by London and Scandinavian Metals Ltd, Rotherham, UK) to the melt, followed by casting10 kg batches into a cast iron mould of 75 mm internal diameter. The 17%Cr white cast irons were produced by laboratory casting. A master alloy of 17%Cr white iron was made in a 10 kg capacity induction vacuum furnace using high purity elements under an argon atmosphere and cast into a metal mould. From this master alloy, 750g samples of material were re-melted in a 1 kg capacity vacuum furnace under an argon atmosphere, and cast at1400°C into steel moulds to produce ingots of dimensions of 2.5×1.5×20 cm. Wear testing was undertaken in both the as-cast and heat treated conditions, with the latter process aimed at destabilising the austenitic matrix. Heat treatment consisted of heating the ingots to 1100°C,holding for 45 min, air cooling to room temperature, then tempering at 250°C for 3 hours. Ingots tested in the 'as-cast' condition were given a stress relief treatment at250°C for 3 hours.

The commercial Duralcan alloy was supplied by Alcan International, Banbury Laboratories, UK. This material had a matrix composition based on the casting grade A357, with 30vol% SiC added by the melt route. The production of the novel Al–6092 alloy–Ni3Al composites was by a powder metallurgy route and is described in detail elsewhere [37]. 6092 aluminium alloy powder, with mean particle size, d50, of 26 μm was produced by inert gas (argon) atomisation and supplied by Alpoco, Sutton Coldfield, UK. Intermetallic Ni3Al powder, supplied by INASMET, San Sebastian, Spain, was obtained by self propagating high temperature synthesis(SHS, for details see [35]). The resulting compact contained97%Ni3Al, which was subsequently

mechanically milled to obtain the powder with a maximum particle size of 50 μm. This powder was blended with the Al powder to give 15vol% Ni3Al reinforcement and then extruded into 12 mm diameter rods at an extrusion ratio of 30:1 at 515°C by Creuzet, Marmande, France. The TiAlN/CrN coating, consisting of alternating TiAlN and CrN layers of thickness 1–1.5 nm, was deposited onto a M2 high speed steel substrate (Vickers hardness 7.99±0.08 GPa) by PVD in a four target HauzerHTC1000-ABS coating machine, using the combined cathodic arc etching and unbalanced magnetron sputtering process, full details of which are presented elsewhere[32].

A variety of counterface materials were used. The316L stainless steel was worn against a commercial magnesia partially stabilized zirconia (Mg–PSZ) disc, supplied by Coors (UK). An M2 tool steel counterface (supplied in bar form by Argent Steel stock holders, Sheffield, UK) was used for testing the TiAlN/CrN coatings, the 17Cr iron, the H21/TiC composites and the Al–alloy/Ni3Al composites. A grey cast iron counterface (supplied by Argent Steel stock holders, Sheffield, UK) was used for the Duralcan tests.

2.2. Wear testing

The 316L and Duralcan tests were undertaken on a tri-pin-on-disc machine, the full details of which are given elsewhere [26]. The rig employs three 10 mm diameter pins with a truncated cone machined at one end, providing a 3 mm diameter contact face. The pins, (316L or Duralcan), were held in a top plate that was prevented from rotating by two half-bridge strain gauges (which provided a measure of the friction coefficient), while the annular disc (Mg–PSZ or grey cast iron) was rotated. The design was such that only 4 mm of the pin projected from the top plate surface in order to ensure maximum system stiffness. The head was placed on top of the disc, located by a central spindle. Loads, in the range 2–60 N/pin (hereafter, all loads quoted are loads/pin), were applied by a dead weight that was secured directly to the top plate containing the pins. All tests were conducted at a constant speed of either 0.24m/s (316L) or 1 m/s (Duralcan). Prior to testing, the surfaces of the pins and the counterface disc were lapped flat and polished to achieve a surface roughness, RA, of less than 0.1 μm. The wear rate was measured by weight loss to an accuracy of ±0.01 mg. Wear tests were run for 10,000 m in most cases (with the exception of the tests where excessive wear was experienced, which were terminated prematurely), and this provided appreciable removal of the pin.

Testing of the H21/TiC, Al–alloy–Ni3Al, 17Cr iron and TiAlN/CrN coatings were undertaken using a Cameron–Plint multipurpose friction and wear testing machine configured for block or pin on disc contact testing. Test blocks of 10mm×10mm×10mm or pins of 7mm diameter were run against an M2 tool steel counterface disc of 60 mm diameter and 10 mm thickness, hardened in the range 800–850 Hv, with a sliding speed of 1 m/s and loads in the range 54–254 N. The coefficient of friction for the couple was recorded throughout each test by means of a load transducer positioned to measure the lateral force on the top shaft. The block and pin sample surfaces were lapped prior to testing in the same manner as the tri-pin-on-disc specimens.

2.3. Transmission electron microscopy of the worn surface

Worn surface samples for transmission electron microscopy (TEM) were produced by both back-thinning and as longitudinal cross-sections. There are a number of different techniques that can be used for the preparation of longitudinal cross-section TEM specimens, well documented in the literature. In the current work, one principal technique was used, first described by Manning and Rowlands [38], later developed by Newcomb and Stobbs [39] and subsequently by the authors[25,26]. A blank piece of the same material as the worn surface was glued to the worn surface using a high strength epoxy resin and allowed to cure for 24 h. 2 mm diameter sections perpendicular to the worn surface were then removed using core drilling (preferably by spark erosion, although mechanical drilling is acceptable for hard materials such as tool steels). This composite rod was then glued into a brass tube of 2 mm internal diameter and 3 mm external diameter. 1 mm sections were then removed perpendicular to the long axis of the composite rod using a slow-speed diamond saw. The discs were then carefully ground to 100 μm thickness, dimpled to 50 μm at the centre of the disc (thinner for hard materials such as tool steels) with a 1 μm diamond paste finish. Samples were then argon ion beam milled to perforation in the conventional manner. Samples were examined in a Philips 420, operating at 120 kV, a Jeol 200CX, operating at 200 kV or a Philips 430 operating at 300 kV. The electron spectroscopic imaging was performed on a Jeol 2010F, operating at 200 kV, equipped with a Gatan imaging filter (GIF), using the procedures optimised by Hofer and co-workers (e.g.[40–42]). The largest possible condenser aperture (200 μm) was used for spectroscopic imaging coupled with high gun emissions(yielding an energy resolution of 1.1 eV), to ensure maximum signal from the small features reported here. The size of the objective aperture (4.8 mrad) was chosen to optimise image resolution. Prior to acquiring spectroscopic images or EEL spectra, a t/l map(t=sample thickness, l=electron mean free path) was taken to ensure that plural scattering could be ignored. Spectroscopic images were obtained using the Fe–M23and Nb–M45 edges. The 3-window method was used to generate elemental maps from which jump ratio images were then computed by dividing the ionisation edge image by a pre-edge image [40]. This removed diffraction contrast and improved signal to noise ratio.

3. Results

3.1. Oxidational wear in ferrous materials

Table 2 summarises the wear data from the tests discussed below. Full details of the wear behaviour are presented elsewhere [25–36]. This section will consider the wear of ferrous alloys, starting with single phase, softer metals, progressing towards the high hardness tool steels and alloy cast irons. It is well known that the load determines the rate of formation and type of surface oxide layers,

Table 2 Lancaster wear coefficients as a function of load for H21 and TiAlN/CrN materials

Material	Lancaster wear coefficient (mm^3/Nm)	Load (N)
H21	18.6×10^{-6}	50
H21	7.5×10^{-6}	254
H21+7%TiC	8.3×10^{-6}	50
H21+7%TiC	10.2×10^{-6}	254
TiAlN/CrN	6.9×10^{-6}	22
TiAlN/CrN	25.8×10^{-6}	91
TiAlN/CrN	24.8×10^{-6}	189

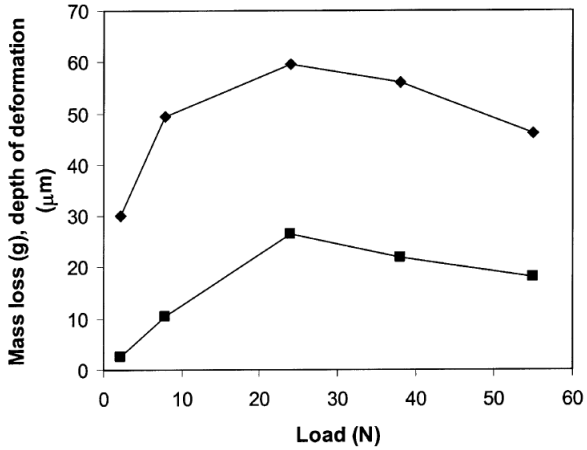

Fig. 1. Plot of mass loss (values×10) (♦) and total depth of deformation (■) as a function of load for the 316L sliding on Mg–PSZ. The reduction of wear and depth of deformation at loads above 24 N is associated with the formation of oxide on the worn surface.

and the consequent effect the oxide has on wear rate (see for example, the classical work of Welsh [23]). Figure 1 gives an example of the beneficial effect of the incorporation of oxygen into the worn surface on the rate of material loss, taken from tests of 316L stainless steel against Mg–PSZ worn in pure sliding in a tri-pin-on disc configuration. The wear, as measured by mass loss, increased with load up to a peak at 24 N, and then decreased with further load. The total depth of deformation(measured using the bending of microstructural markers [25,43]), followed the same trend. Backscattered imaging of the worn surface revealed darker regions, Fig. 2, the proportion of which increased with load. EDS of the darker regions in Fig. 2 indicated that they contained a significant proportion of oxygen, but otherwise retained the same ratio of Fe:Cr:Ni as in the surrounding areas. Such features have been described as 'oxide' by other researchers (e.g. [44]), although as shown below, the situation is more complex in the current case.

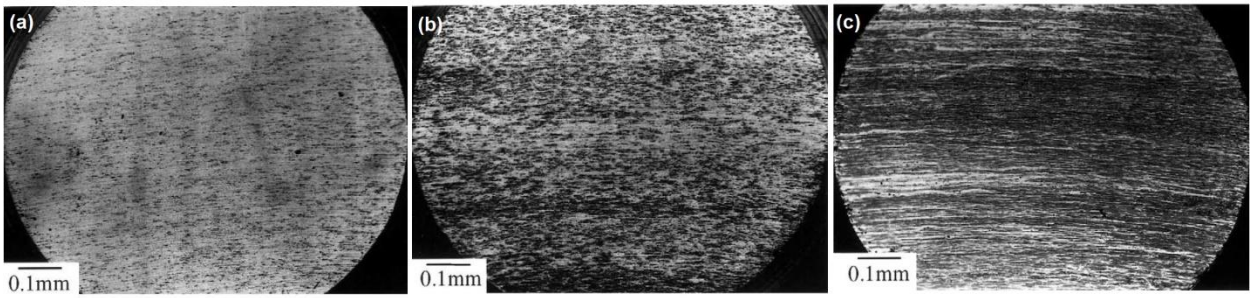

Fig. 2. Back scattered electron micrographs of the worn surface of an AISI 316L stainless steel, tested against an Mg–PSZ counterface at 0.24 m/s. (a) 2.2 N; (b) 24 N; (c) 55 N. Note the increased coverage of oxide (dark areas) as the load increases.

Figure 3(a) shows a detail from Fig. 2, from the worn surface from the 316L test at 6.8 N, showing a prow that had apparently been pushed through the surface, leaving a groove in its wake. EDS of the regions of the prow giving dark contrast in the backscattered electron image indicated that they contained oxygen. XRD of the worn surface failed to reveal any additional peaks other than austenite. These prows were frequently found to be a source of wear debris, as shown in Fig. 3(b). At the highest test load, the number of prows substantially decreased,

replaced by a continuous film of the oxygen containing phase, which was frequently cracked, Fig.3(c).

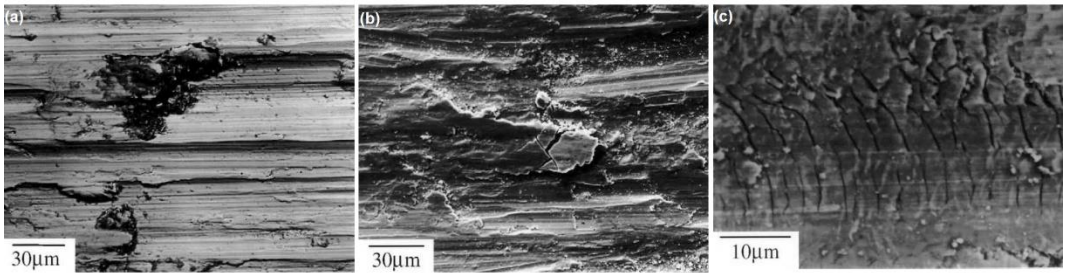

Fig. 3. SEM micrographs of the worn surface of a 316L after dry sliding against a partially stabilized zirconia counterface (Mg–PSZ) at loads in the range 2.2–55 N and 0.24 m/s. (a) Back-scattered electron image of a prow formed at 2.2 N, apparently a mixture of metal (light) and oxide (dark); (b) secondary electron image of wear debris formed at a prow containing appreciable oxide after testing at 24 N; (c) backscattered electron image of region of continuous oxide formed at 55 N, showing widespread cracking.

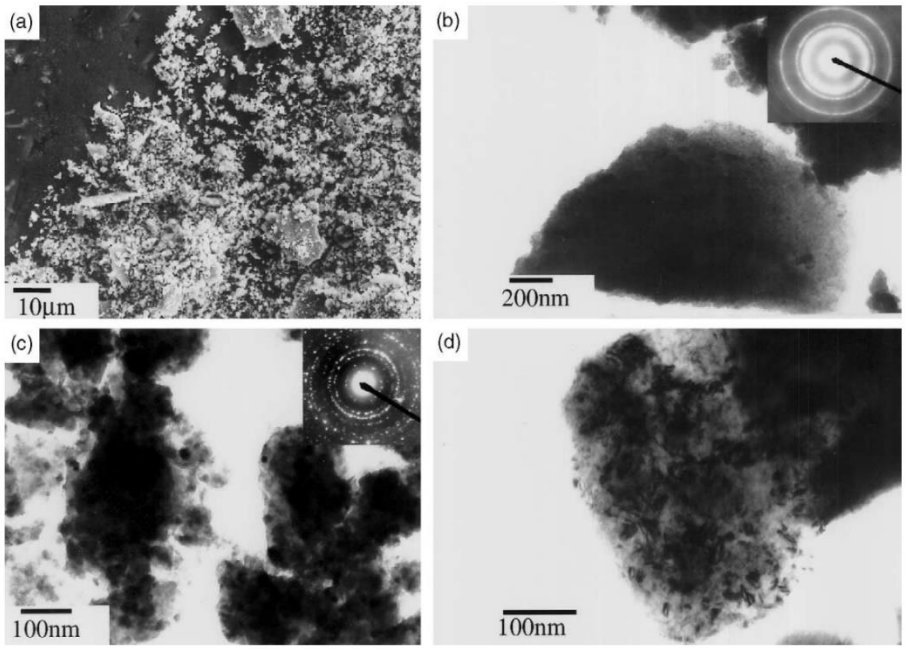

Fig. 4. Images of the wear debris from the dry sliding of 316L against a partially stabilized zirconia counterface (Mg–PSZ) at a load of 55 N and speed of 0.24 m/s. (a) SEM micrograph showing the morphology of the wear debris; (b) TEM bright field micrograph of a particle that contains both an amorphous phase and the non-equilibrium bcc phase, both of which contained oxygen; (c) TEM bright field micrograph of Fe3O4 particles; (d) TEM bright field micrograph of a heavily deformed g-Fe particle.

The wear debris consisted mainly of fine, roughly equiaxed, particles, Fig. 4(a). XRD of the wear debris indicated that it contained several phases, including g-Fe (i.e. metallic wear from the 316L), a small amount of α'-Fe (only at the lowest load of 6.8 N), occasional Fe3O4 peaks (loads of 24 N and above), a significant amorphous component and also a body centred cubic(bcc) phase that could not be identified in the JPDS files(with distinctly different lattice

spacings to a————————————————-Fe).Wavelength dispersive X-ray analysis of the wear debris, using an electron probe micro analyser (EPMA), indicated that the debris generally contained substantial quantities of oxygen,

Table 3 WDS analysis of the wear debris from the 316L tests on Mg–PSZ

Load(N)	Fe	Cr	Ni	Mo	Si	Zr	O
2.2	49.3	12.2	8.76	1.7	0.14	0.42	27.4
55	48.7	12.1	8.78	1.7	0.15	2.24	26.2

and that the composition did not vary appreciably with load, Table 3. Interestingly, a small quantity of Zr was found in the analysis, the proportion of which increased with load.

TEM of the wear debris (Fig. 4(b)–(d)) confirmed the presence of the phases found by XRD. An example of the amorphous and non-equilibrium bcc debris is shown in Fig. 4(b), a Fe3O4 particle in Fig. 4(c) and a metallic particle of g-Fe is shown in Fig. 4(d). Interestingly, some of the amorphous and non-equilibrium bcc debris recrystallised under a focused electron beam, transforming directly to Fe3O4. No evidence of ZrO2 particles could be found, although interestingly, EDS suggested that the amorphous and non-equilibrium bcc debris contained Zr in solid solution. Regrettably, the relative proportions of each phase could not be determined because a proportion of the wear debris was not electron transparent, while proportions could not be measured by XRD because of the high background levels, the extensive peak broadening and the absence of standards. XRD showed that heating the wear debris at 350°C for 1 h in air initiated some transformation of both amorphous and bcc phases toFe3O4, while heating at 450°C for 1 h produced complete transformation to Fe3O4. While some oxidation could clearly have occurred during heating of the wear debris, this does suggest that surface temperatures during wear testing were below 350°C.

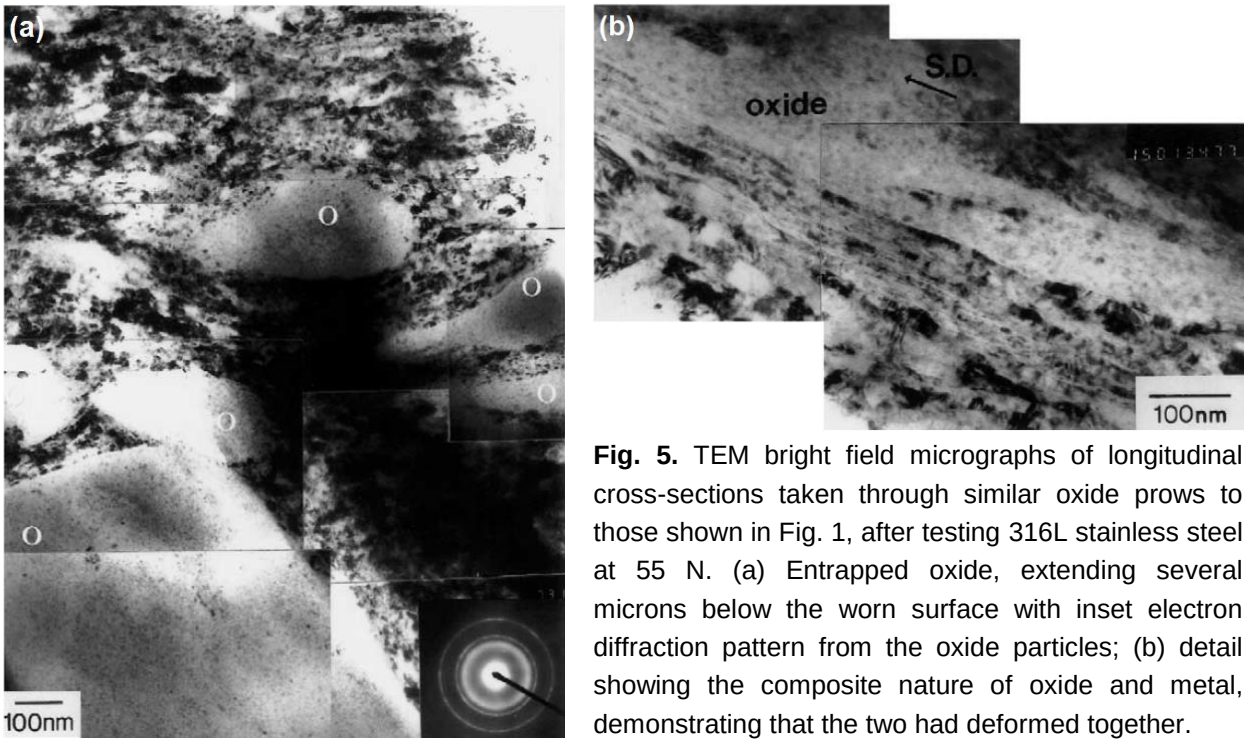

Fig. 5. TEM bright field micrographs of longitudinal cross-sections taken through similar oxide prows to those shown in Fig. 1, after testing 316L stainless steel at 55 N. (a) Entrapped oxide, extending several microns below the worn surface with inset electron diffraction pattern from the oxide particles; (b) detail showing the composite nature of oxide and metal, demonstrating that the two had deformed together.

Figure 5(a) gives a TEM image through a prow, similar to that shown in Fig. 3(a). The microstructure consisted of the same oxygen-containing particles (labeled 'O' in Fig. 5(a)) as found in the wear debris, distributed through a heavily deformed matrix. Electron diffraction and EDS indicated that the phases present in these samples were similar to those in the wear debris, although no Fe3O4 was found embedded in the surface layers. The non-equilibrium bcc phase constituted the majority oxygen-containing phase present, with only relatively small amounts of the amorphous phase present. The grain size of the non-equilibrium phase was of the order of 5 nm, but was generally too small to measure quantitatively with any confidence. The metallic matrix was entirely austenitic, with no evidence of strain-induced martensite (α'-Fe) being found, either in the diffraction pattern or from the characteristic appearance of a strain-induced martensite. The subgrain size in the matrix was extremely fine, being as small as 12±8 nm at the surface (the detailed aspects of the matrix deformation are discussed elsewhere [25]).

The bright field TEM image in Fig. 5(a) shows clear evidence of the strain discontinuity between oxygen-containing phase and matrix, with the matrix undergoing locally much greater strain where it flowed around the harder oxygen-containing particles. The non-metallic fragments appeared to have originated from break-up of the surface oxygen-containing film such as that in Fig.3(c), which became incorporated into the structure well below the contact surface as a result of severe plastic deformation and associated microstructural rotation.

Close examination of the microstructure nearer to the surface indicated that deformation of the oxygen-containing phase had also occurred, for example, fragments of this phase had become elongated in the sliding direction, Fig. 5(a). In places, the deformation of the oxygen-containing phase was substantial, Fig. 5(b), with the plastic deformation in both oxygen-containing phase

and matrix resulting in a nanoscale composite structure, with intimate mixing with the g-Fe. There was no evidence of cracking at the interface between the various phases, either in the heavily deformed regions of Fig. 5(b) or the entrapped oxygen-containing particles in Fig. 5(a). While SEM indicated microscopic cracking (Fig. 3(c)),such regions would have probably been lost during TEM preparation and therefore the origins of such cracks could not be studied in detail. An H21 tool steel, containing a range of TiC particle contents up to 7wt%, was tested in pure sliding against an M2 tool steel. In general, the wear coefficient decreased with an increase in load, associated with an increase in the oxide content of the surface. However, this effect was less as the volume fraction of TiC was increased. Table 2 gives the wear data for the unreinforced H21 and the H21+7%TiC.

Figure 6 gives a TEM micrograph taken from the extreme worn surface of an H21+7%TiC tool steel tested against an M2 tool steel counterface in unlubricated sliding at 1 m/s and 254 N. The martensitic matrix had transformed to α-ferrite, which had become extensively deformed. Unlike the case of the 316L stainless steel in Figs 4 and 5, the oxide could be identified, and was found to be predominantly Fe3O4. However, the oxide exhibited many similarities to that observed in the 316L, for example, it exhibited intimate mixing with the metallic matrix, with no evidence of cracking at the interface between the two phases. In common with the oxide in the stainless steel, there was evidence that the oxide itself had also been deformed in places, forming a nanoscale

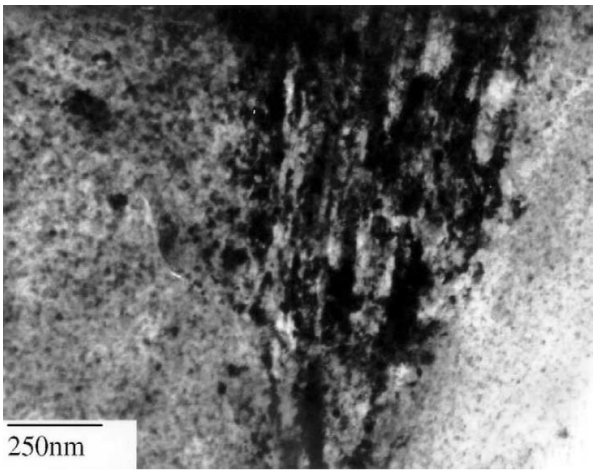

Fig. 6. TEM bright field micrograph from back thinned samples of the worn surface of a H21+7% (WTiC) tool steel, worn against M2 tool steel in pure sliding at 254 N, 1 m/s, showing apparent co-deformation of a a-Fe (subgrains-size 33±25 nm) and the oxide structure (predominantly Fe3O4 of size 15±13 nm).

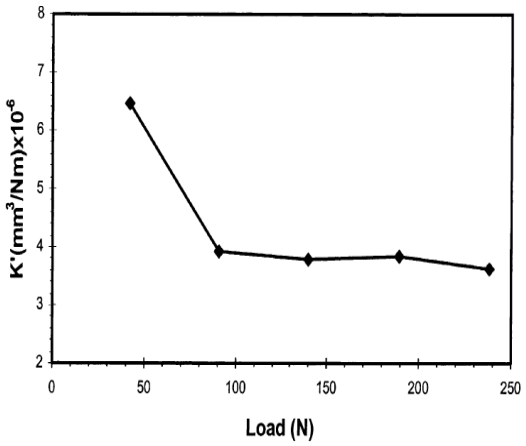

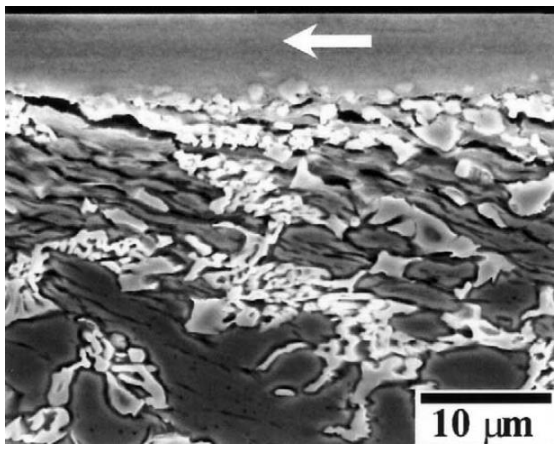

Fig. 7. Wear coefficient as a function of load for a 17% Cr white cast iron worn against an M2 tool steel.

Fig. 8. SEM micrograph of the worn surface of a 17% white cast iron worn against M2 tool steel at 28 N and 0.94 m/s, showing a thick oxide surface layer. Note the fragmentation of the M7C3 just below, and the incorporation of this carbide into the bottom of the oxide layer.

composite (compare Figs 5(b) and 6), although the extent of this was much less than observed for the 316L stainless steel. Moreover, the oxide crystallite size was very fine (15±13nm) as was the sub-grain size of the α-ferrite (33±25 nm),but there was no preferred crystallographic orientation detected within the oxide.

A 17%Cr white cast iron was tested in the same test rig, with the same counterface and sliding speed as the H21 tool steel described above, but with a slightly different load range. Figure 7 shows the wear coefficient as a function of load. The highest wear coefficient was recorded at the lowest load (42 N), but for loads of 91N and above, the wear coefficient was approximately constant. The reduction in wear coefficient was associated with a change in wear mechanism. At the lowest load, an intermittent, thin, oxide film was present, and a significant fraction of the wear debris was metallic. For loads of 91 N and above, the surface was covered in a uniform oxide film, the thickness of which increased with load. Figure 8 shows an SEM micrograph of the oxide film at the highest load of 238 N, where it was typically 10 μm thick. In addition, the phase constitution

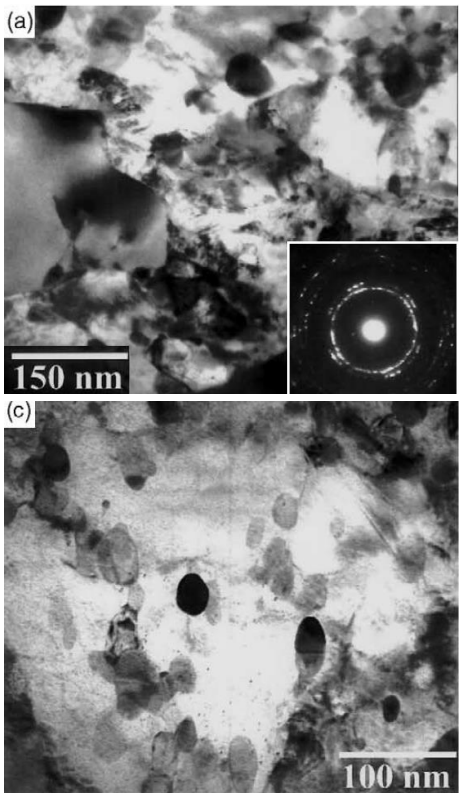

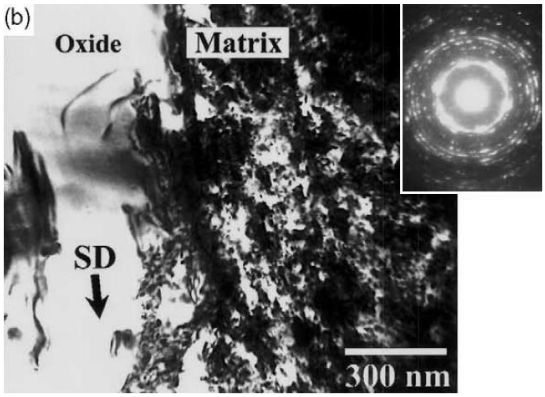

Fig. 9. TEM bright field micrographs from back thinned samples of the worn surface in Fig. 5, showing (a) fragmented M7C3 carbides just below the oxide layer; (b) the oxide/heavily deformed matrix interface; and (c) carbide particles within the thick Fe3O4, Fe2O3 oxide layer.

of the oxide changed with load, being only Fe2O3 for loads up to 91 N, but Fe2O3 and Fe3O4 for the higher loads.

Figure 9 gives TEM micrographs from various positions below the worn surface shown in Fig. 8. Figure9 (a) shows fragmentation of the carbide below the worn surface, within a heavily deformed matrix. Interestingly, there was minimal cracking between carbide fragments and the matrix, although, as noted above, regions that are cracked tend to be lost from TEM samples during specimen preparation. Figure 9(b) shows the interface between the oxide and matrix, which was found to be abrupt, but again free from cracking. In contrast to the oxide observed on the surface of the stainless steel and the H21 tool steel, the grain size of the Fe3O4 seen in this micrograph was comparatively coarse(approximately 100–300 nm). Figure 9 (c) shows the microstructure within the thick oxide film. It contained fine carbide fragments, 5–20 nm in size, located principally along the oxide grain boundaries (Fe3O4 in this example). These particles were found throughout the oxide film, even though they had not been resolved in the SEM micrograph in Fig. 8.

3.2. Formation of oxides in the wear of aluminium alloys

In contrast to the ferrous materials, the wear coefficient of alumium alloys often shows an increase with an increase in load. Figure 10 shows the wear coefficient of a Duralcan Al–Si–SiC alloy as a function of load. The increase in wear coefficient was related to fragmentation of the SiC at the worn surface and subsequent classical delamination resulting from easy growth of cracks through the matrix from particle to particle, with cracks initiated at the reinforcement/matrix

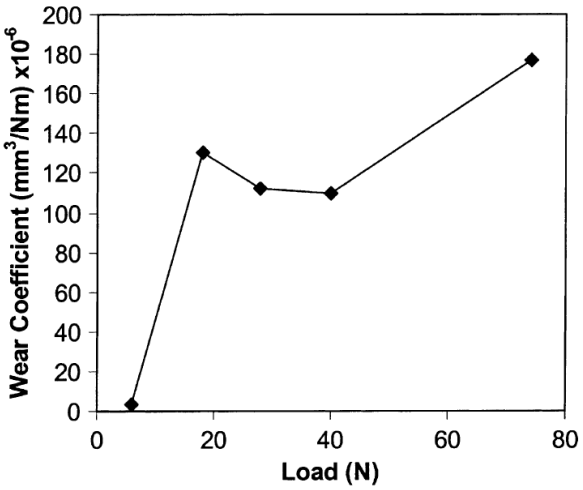

Fig. 10. Wear coefficient as a function of load for Duralcan (Al–Si–SiC) worn against a grey cast iron at 1 m/s in pure, unlubricated, sliding.

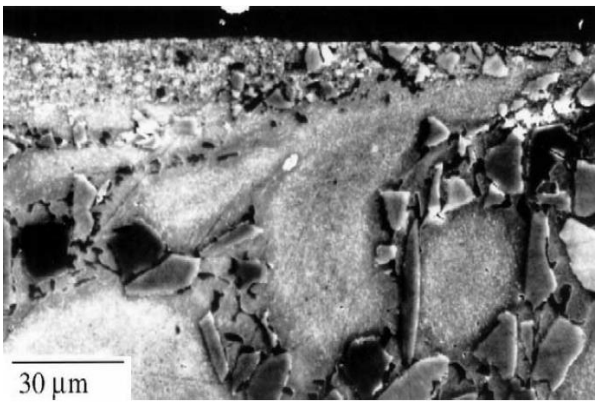

Fig. 11. SEM micrograph of a longitudinal cross-section of a Duralcan (Al–7.6wt% Si–0.5wt% Mg–30vol% SiC) composite worn against grey cast iron at 40 N and 1 m/s, showing fragmentation of the SiC, transfer from the disc, but no apparent oxidation of the aluminium.

interface [28]. Figure11 gives an SEM micrograph of a longitudinal cross-section of the Duralcan worn against a grey cast iron counterface at 40 N and 1 m/s, which shows the fragmentation of the hard second phase particles (Si and SiC) that is the precursor to surface delamination. SEM examination of the worn surface in plan view revealed extensive surface grooving and transfer of Fe from the grey cast iron counterface. Interestingly, SEM suggested that the Fe had become oxidized while there was no evidence of oxidation of the Al.

Figure 12 gives bright field TEM micrographs of the worn surface shown in Fig. 11. The structure was complex, comprising several different phases as well as a heavily deformed a-Al matrix. There was widespread cracking within the structure, particularly at the interface between particles and matrix. Of particular interest was the dominance of α-Al2O3 in addition to the fragmented Si and SiC particles. The α-Al2O3 exhibited an ultra-fine structure, Fig. 12(b). While in some places the grains were randomly oriented, Fig. 12(a), in other regions the α-Al2O3 crystallites were slightly elongated with the long dimension following the profile of the particle edge, Fig. 12(b), although their crystallographic orientation remained random.

The wear of Al alloy–SiC composites is dominated by the high hardness of the SiC and the delamination wear that is common at high loads, induced by particle fracture and ductility exhaustion at the interface between particle and heavily deformed matrix [25], and by the abrasive action of the SiC on the counterface. In an attempt to reduce these effects, an Al-based composite reinforced with a Ni3Al particulate, that is substantially softer than SiC, was developed, the full

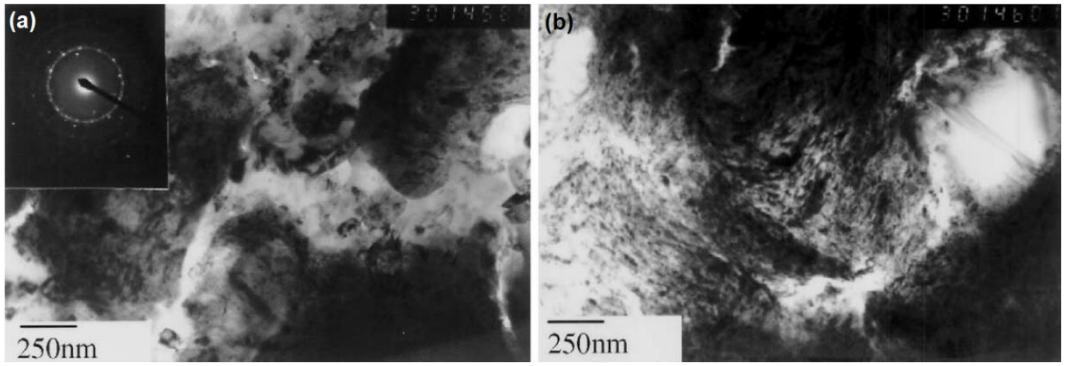

Fig. 12. TEM bright field micrographs from a back thinned sample of the worn surface shown in Fig. 10. (a) Fragmented particles, comprising predominantly α-Al2O3, but also SiC, within a heavily deformed a-Al matrix; (b) detail of an a-Al2O3 particle, showing ultra-fine substructure.

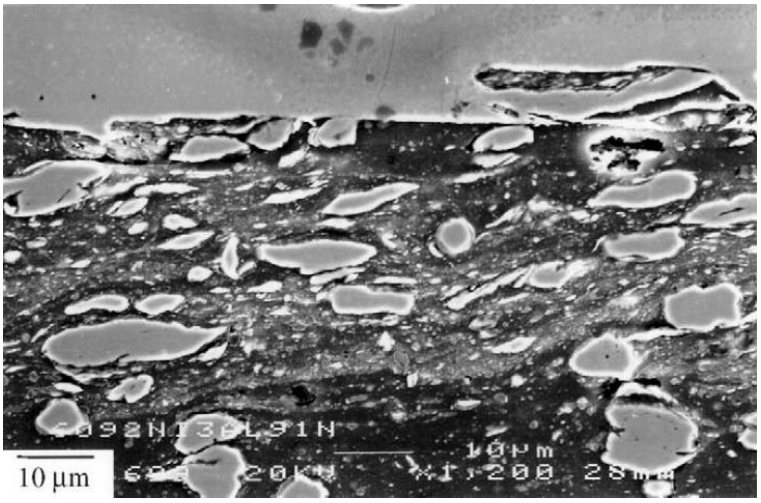

Fig. 13. SEM micrograph of a longitudinal cross-section of a novel Al–6092–30vol%Ni3Al composite worn against an M2 tool steel at 91 N and 0.94 m/s, showing fragmentation and deformation of the Ni3Al.

details of which are reported elsewhere [35,37]. Figure 13 gives a longitudinal cross-section from the test at 91 N, 0.94 m/s against an M2 tool steel counterface. This load is above a critical maximum at which the reinforcement becomes plastically deformed and fragmented. However, as shown in Table 2, this did not result in an increase in wear coefficient. The reason for this was believed to be because a mechanically mixed layer (MML) was built-up at the surface, comprising components of both counterfaces, which was considerably harder than the Al composite substrate. Figure 14 gives TEM micrographs of a longitudinal cross-section through the worn surface shown in Fig. 13, but from a region where the MML was more extensive. The structure of the MML was found to be complex and was made up of a number of phases. In addition to heavily deformed a-Al (Fig. 14(a)) and fragmented Ni3Al (Fig. 14(b)), an amorphous phase was present that contained both Fe and Al, but with appreciable quantities of oxygen (Fig. 14(a)). This phase contained fine, nanoscale, cracks and was present in several different morphologies, ranging from elongated to equiaxed.

It is extremely difficult to evaluate the phase distribution from bright field TEM micrographs such as those in Fig. 14. Dark field imaging has only limited use since the diffraction rings of the different phases were frequently too close to allow an image of an individual phase to be obtained.

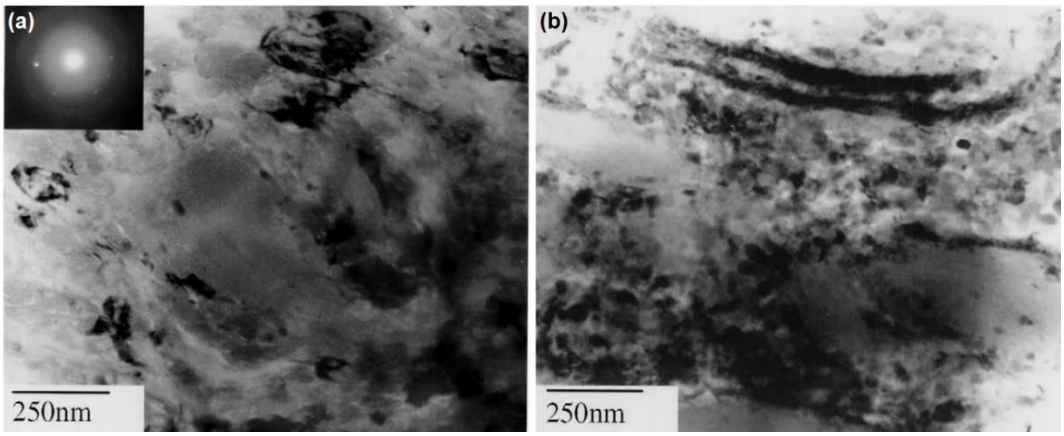

Fig. 14. TEM bright field micrographs of longitudinal cross-sections taken through the worn surface shown in Fig. 9. (a) Showing the complex structure of the MML. The selected area diffraction pattern shows an amorphous component (labelled A), fine a-Al crystallites and an Fe,Al,O containing phase (labelled B) that contained fine (~10 nm) crystallites within; (b) a similar region to (a), but containing deformed Ni3Al particles.

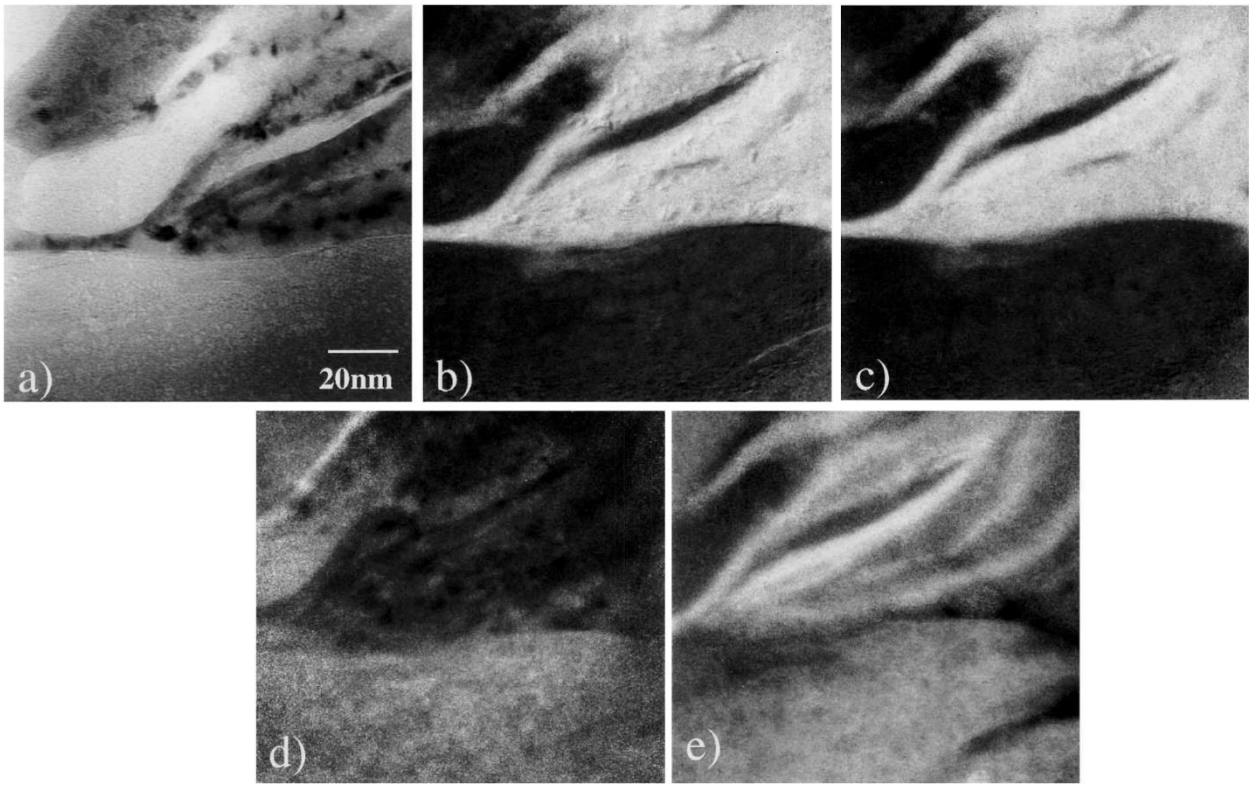

Fig. 15. Energy filtered TEM images (jump ratio) from the sample shown in Fig. 10. (a) Zero loss filtered bright field TEM; (b) Al map; (c) Ni map; (d) O map; (e) Fe map. Note the intimate scale of mixing.

In order to gain a better understanding of the phase distribution, electron spectroscopic imaging was used. This technique has been widely used to study chemical distribution in metallic and ceramic systems (e.g. [40–42]), but has not been used to evaluate worn surface structures. Fig. 15 gives elemental distribution maps (jump ratio images) taken from one region close to that in

Fig. 14(a). Figure 15(a) gives a brightfield TEM image after removal of the inelastically scattered electrons (in other words, this is a 'pure' diffraction contrast image). The lower region comprised the amorphous Fe–Al–O phase observed in Fig. 14(a). The middle feature was positively identified as Ni3Al. The feature in the upper left region could not be positively identified. Figure 15(b, c) give Al and Ni maps, respectively, and are consistent with the identification of Ni3Al.Figure 15(d, e) are consistent with the earlier analysis that shows the amorphous phase contains Fe and O. Note also that the contrast shown is relative, and by adjusting the contrast scale, it was clear that the lower region also contained Al, albeit in small quantities. Interestingly, the Ni3Al also contained Fe, intimately mixed within, as shown in Fig. 15(e). The phase in the upper left hand corner also contained Fe and O, with some Al, and appeared to be a nanocrystalline form of the amorphous phase.

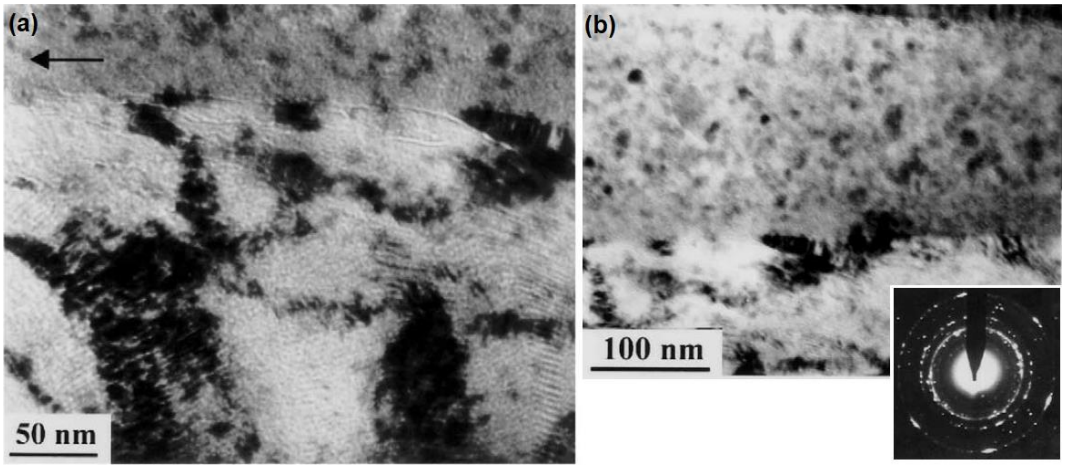

Fig. 16. (a) Bright field TEM micrograph from a longitudinal cross-section of TiAlN/CrN worn against an M2 tool steel counterface at 0.42 m/s and 91 N showing deformation and a surface transfer film. The arrow indicates the direction of movement of the counterface (the coated sample was static). The Fresnel contrast reveals the position of the multilayer structure and the microcracks; (b) detail from (a) showing the transfer film, predominantly made up of Fe3O4. The thin feature at the top of the micrograph is a gold coating used to label and protect the original surface.

3.3. Formation of oxides in the wear of TiAlN/CrN coatings

Coatings have been used for some time to enhance the wear resistance of tooling, in particular, cutting and milling tools. The latest 3rd generation coatings are based on a nanoscale multilayer structure (hence their name 'superlattice' coatings), and offer the exceptionally high hardness (consequently, they are often called 'superhard' [32]). The combination of high hardness, excellent thermal stability and good oxidation resistance offers the potential for these coatings to be used in unlubricated high speed cutting applications. As such, the oxidational wear mechanisms are of particular importance.

Figure 16 gives bright field TEM micrographs from a longitudinal cross-section from a TiAlN/CrN coating. The surface was covered in a thin polycrystalline layer, typically 100–300 nm thick. Electron diffraction and EDS indicated that the film was predominantly Fe3O4but with some Al2TiO5 and trace quantities of the components of the TiAlN/CrN. In common with the

iron based oxides observed on the 316L and H21 worn surfaces, the structure of the oxide layer was in the nanostructure regime, with an average crystallites size 11±5nm. The interface between this surface layer and the deformed substrate was always found to be sharp, with no transition region detected.

Below the surface oxide layer, the superlattice coating had been plastically deformed to a depth of 55 nm (seen clearly by the bending of Fresnel contrast from the individual layers). The plastic deformation resulted in the formation of fine cracks, which appeared to be the precursor to delamination, which presumably resulted in the pitting seen elsewhere on the surface.

4. Discussion

4.1. Comparison of test conditions

It is important that microstructural observations be putin perspective with respect to the operative wear mechanisms. Since the wear mechanism descriptions used in the literature are generally subjective, the most convenient method to compare test conditions is to use the normalised pressure and normalised velocity as defined by Lim and Ashby [24], which also allows the current conditions to be compared to the wear mechanism maps[24], (although Lim and Ashby cite data for a range of steels, from carbon to tool steels, but do not include stainless steels). For the wear tests on the 316L the normalized pressure, F˜ , was in the range $3–24\times10^{-5}$, while the normalised velocity, v˜, was 132. The corresponding values for the H21+7%TiC and 17%Cr Fe are $F3\times10^{-4}$ and v˜524 (figures are approximate, since thermal diffusivities of these materials are not known exactly, however, small errors make no difference to the regimes shown in the wear maps). A comparison of the these figures with the Lim and Ashby maps (bearing in mind the compositional differences, particularly for stainless steels) and the published literature on the wear of steels suggests that the stainless steel should be operating within the Archard adhesive wear regime, while the H21+7%TiC and 17%Cr iron were operating firmly within the mild oxidational wear regime(or ‘mild wear’) defined by Quinn.

The corresponding figures for the Duralcan are F˜2.5×104 and v˜69, while the Al–alloy–Ni3Al composite yielded $F˜\ 5.7\times10^{-4}$ and v˜69 (again, no account is taken for the small difference in thermal diffusivity between an Al–Si matrix for the Duralcan and the 6092matrix for the Al–alloy–Ni3Al composite). These values can be compared to the Al wear mechanism map proposed by Antoniou and Subramanian [45], and suggest that the Al–alloy/steel couples are operating in the mild wear regimes. The differences in F˜ and v˜ between the steel and aluminium tests are comparatively small (2×for the 316L, 7.6× for the H21+7%TiC and 17%Cr iron),certainly small compared to the 6 orders of magnitude range in test conditions reported in the literature on, for example, carbon steels [24].

4.2. The role of oxygen in the wear of 316L

The literature on oxidational wear has largely assumed that only equilibrium oxide phases are formed by the wear process. For example, Smith [46–48] observed a-Fe2O3 for the reciprocating and sliding wear of self-mated 316 stainless steel in the temperature range 20–

500°C. Similar tests in CO2 [49] introduced Fe3O4 in preference to a-Fe2O3 at room temperature, but both phases at 300–500°C. Tests of the same material in pure sliding yielded a hydrated form of hematite (d-FeOOH),although the experimental XRD data did not exactly match the corresponding JPDS file [46]. Saito et al. [44]observed an 'oxide' (based on Electron Probe Microanalysis(EPMA)) in the sliding of 316L under severe sliding conditions of 50 ms1, 1.88×103–1.18×104 N, for temperatures up to 260°C. The current results have found non-equilibrium phases that retain the same ratio of Fe:Cr:Ni as in the 316L, but contain appreciable quantities of oxygen (25 weight %). The dominant constituent was a non-equilibrium, oxygen-containing bcc phase, with a crystallite size average in the range 5–10 nm, but this was interspersed with an amorphous phase of the same composition. Observations of amorphous and nonequilibrium phases have been made in high energy mechanical milling (e.g. [50]), but there has only been a few reports of non-equilibrium oxide phases formed during wear (e.g. de Wit et al. [51] reported amorphous tin oxides during the sliding wear of tin against corundum, Li and Tandon [52] observed an amorphous aluminium phase containing appreciable quantities of oxygen after sliding an Al–Si/SiCp composite sliding against a bearing steel and finally Wang et al. [53] observed anamorphous phase at the surface of a bearing steel). It is not clear why the current observations differ from those in the literature on stainless steels, except that in the current work a ceramic counterface was used, rather than metal on metal couples predominantly used elsewhere. However, the difference may be that the current observations were based on detailed TEM analysis, and the resulting identification could not have been obtained from XRD alone, because of the substantial peak broadening that arose from the ultra-fine grain sizes. It is interesting to note that the identification of d-FeOOH made by Smith [46] was not precise (because of similar difficulties of X-ray line broadening), and that the lattice spacings of d-FeOOH are similar to the non-equilibrium bcc phase observed in the current study. Moreover, it is far from clear why a hydrated phase should form in a system where the driving force to produce equilibrium oxides is high, and the frictional heating at the worn surface would probably be significant.

The nanocrystalline non-equilibrium bcc and amorphous oxygen-containing phases partially transformed to equilibrium phases on heating at 350°C for 1 h, while heating at 450°C for 1 h produced complete transformation to Fe3O4. While there will have been a difference between oxygen partial pressure on heating in air, and adjacent to the contacting asperities, this observation suggests that the oxide was formed at a temperature well below 350°C, consistent with the predictions of flash temperature that suggested a probable temperature rise of 200–250°C [25].

No strain-induced martensite (α'-Fe) was found in TEM studies of the worn surface, while X-ray diffraction of the wear debris suggested a small fraction of this phase was formed at 6.8 N, but not at higher loads. Observations of α'-Fe are common in the sliding wear studies of stainless steels (e.g. [54,55]), although many of the observations have been made on 310 and 304stainless steels, which have a significantly higher martensite-start temperature than 316 stainless steel and therefore transform much more easily than 316 stainless steel during wear tests. While the number of studies on316 stainless steel is relatively small, α'-Fe formation has

also been observed in reciprocating wear of 316 on316 by Smith [49]. In the current studies, type 316 stainless steel was chosen specifically because it is a more stable alloy than types 304 and 310. Moreover, the use of a low thermal conductivity zirconia counterface will have resulted in higher flash temperatures than would have occurred in the tests of Smith. The martensite start temperature (Ms) for strain-induced transformation in316 has been reported as 68°C by Cook [56], which is below the expected surface temperatures in the current test 200–250°C [25], but clearly above the surface temperatures in the air tests of Smith [46–48]. Thus, the absence of a-Fe in TEM cross-sections is consistent with the predicted Ms for this material and the predicted flash temperatures.

Figure 3(a) shows a prow, which forms the contacting asperity, on the surface of the worn 316L stainless steel. The backscattered electron imaging in Fig. 3(a) and TEM examination in Fig. 5(a) show that the prow was a complex mixture of the oxygen-containing phases and the parent metal, that had become intimately mixed as a result of severe plastic deformation and associated lattice rotation and particle fragmentation. Figure 3(b) shows the liberation of a wear particle from such a prow. The sequence of events shown in these images is in broad agreement with the sequence described by Quinn [10].However, there are important differences between the mechanism observed in Fig. 3 and the classical oxidational wear mechanism. The first is shown in the TEM images in Fig. 5. In this case, the oxide was intimately mixed with the matrix. In addition, the oxide had been deformed; in places the co-deformation of the oxide and metal created a complex composite structure. This contrasts strongly with the classical model that is based on a uniform oxide layer. However, this comparison may not strictly be fair. In Sullivan et al.'s [8] tests using anEN8 steel, for example, the worn surface was reported to be comparatively smooth, and the wear system exhibited all the characteristics of mild wear. In contrast, the316L tests reported here exhibited some aspects of severe wear, namely, extensive ploughing of the surface, presumably because the 316L is comparatively soft in comparison to EN8. Based on normalised pressure, the316L was operating in the 'oxidational wear + ploughing' regime identified by Rapoport [20], whose wording suggests a slightly more severe condition than the mild wear regime of Quinn.

Despite the differences in type and morphology of oxide (or oxygen-containing phase) formed, there was one important similarity between the present tests on316L and the EN8, namely that, provided the type of oxide did not change, the Lancaster wear coefficient [57](mm3/Nm) decreased with an increase in load. The extent of this change was far greater in the current tests on 316L, and was clearly associated with an increase in the fraction of the surface covered in oxide. Thus, the oxide improved the wear resistance of the material. Within the context of the classical oxidational theory of wear, the perceived reasons for a reduction in wear coefficient with an increase in the oxide presence is because of a reduction in adhesive forces, rather than an improvement in surface mechanical properties. Indeed, Quinn[10] suggests that the true contact area is determined by the mechanical properties of the metal substrate rather than the mechanical properties of the oxide. The present results demonstrate that this is not the case for the 'oxidational wear + ploughing' reported here. In contrast, it is proposed that the improvement in wear coefficient arises because the oxide is essentially

mechanically mixed with the surface (a mechanically mixed layer or MML [58,59]), forming a hard metal matrix composite that has superior wear resistance to the comparatively soft γ-Fe matrix. This point will be developed further when thewear behaviour of the tool steel and white iron is considered.

4.3. Oxidational wear in the tool steel and white iron

The worn surface of the H21+7%TiC tool steel conformed closely to the definition of mild wear, exhibiting a comparatively smooth worn surface with wear debris that was generally sub-micron and predominantly oxide. Moreover, as noted above, the Lim and Ashby wear map predicted mild oxidational wear for these test conditions .As with the 316L, a decrease in Lancaster wear coefficient with increase in load was associated with an increase in oxide coverage of the surface. Nevertheless, the surface had undergone major structural change, in particular, the martensitic matrix had transformed to a-Fe and had been plastically deformed to high strain. As shown in Fig. 6, the oxide was predominantly Fe3O4with a nanocrystalline structure that led to substantial line-broadening in X-ray traces (this is another interesting example of where phase identification was substantially easier by TEM than by X-ray diffraction).

The behaviour of the oxide showed two important similarities with that observed for the 316L. Firstly, the oxide had become intimately mixed with the metal matrix, locally forming a composite structure. While this was by no means as extensive as in the 316L, it was nevertheless a distinctive feature. Moreover, for theH21+7%TiC, the composite structure also included carbides and fragments of the TiC particles. Secondly, the oxide formed had an ultra-fine structure, well within the nanocrystalline range. Such structures are known to have unique properties when compared to their microcrystalline counterparts, for example, showing enhanced strength and ductility [60]. This ultra-fine structure and the intimate mixing of the oxide and metal matrix makes an estimate of the mechanical properties of the surface layer difficult, although nano hardness testing should further extend our understanding in the future. Interestingly, the wear coefficient data suggests that this structure provided superior wear resistance compared to the quenched and tempered martensite starting structure.

In common with the 316L and the H21+TiC tool steel, the 17%Cr white iron exhibited a decrease in wear coefficient with load, associated with the formation of an oxide. At the lowest load of 42 N, the wear was predominantly metallic, while at 91 N and above the worn surface was covered in a continuous oxide film. Despite the identical test conditions used for the H21+7%TiC and white iron tests, the oxide morphology found on the two surfaces was quite different. The oxide film on the white iron was continuous and therefore was not located predominantly at the contacting asperities, Fig. 8. The film, up to 10 μm thick, could be described as a ‘glaze’ as observed, for example, on the worn surface of Ni-based superalloys (e.g. [61–64], although such glazes often comprise compacted oxide wear debris and are often only observed in tests where the bulk temperature of the sample is artificially raised). There was no evidence of mechanical mixing of the white iron substrate and oxide film. Given the similarity in test conditions betweenH21+TiC tool steel and 17Cr white iron (geometry, counterface, load

range and speed), the difference in oxide morphology must arise from the differences in material properties.

For loads up to 91 N, the oxide on the white iron was only Fe2O3, but Fe2O3 and Fe3O4 were present at the higher loads. This suggests that the asperity contact temperature was not the reason for the difference in oxide film morphology, since only Fe3O4 was observed on the surface of H21+7%TiC, i.e. the results indicate that surface contact temperature was higher for the H21+7%TiCthan for the 17%Cr white iron. Thus, there must be an alternative mechanism to explain the difference in oxide morphology.

As discussed above, the surface of the H21+7%TiChad transformed from martensite to a-Fe, which had been severely plastically deformed. An equivalent tensile strain of 8 was measured at the surface (using lines of segregation present in the cast structure that were initially perpendicular to the worn surface), with a total depth of deformation of 13 μm. The corresponding figures for the 17%Cr iron was an equivalent tensile strain of 3.5 and a total depth of deformation of 15μm [36]. Thus, the total depths of deformation were similar, but the H21 had undergone about twice the strain at the surface compared to the 17%Cr iron, not surprising given that tool steels generally have sufficient ductility to be hot worked, while white irons do not. However, failure of the oxide film is often believed to be at the substrate/oxide interface [10]. A stable glaze layer can only be established where the strain discontinuity between oxide and substrate is small, i.e. substantial ductility of the substrate will result in mechanical mixing of the oxide (as shown by the 316L) rather thana thick glaze layer. It would appear therefore, that the surface strains for the 17%Cr white iron were sufficiently small to allow a glaze layer to be formed, while for the H21+7%TiC, the strains were too high, and a degree of surface mechanical mixing occurred. Interestingly, a glaze layer is observed on the surface of 17%Crwhite iron hot mill work rolls, which periodically detaches, resulting in poor workpiece surface quality where the oxide has become incorporated into the workpiece surface [22].

4.4. Oxides of the surface of the aluminium alloys

Oxidation has not been regarded as an important mechanism in the wear of aluminium alloys, although Li and Tandon [65,66] found alumina as a minor constituent in a mechanically mixed layer formed from the sliding of Al–Si alloys on steel. The absence of oxides on the worn surface of aluminium is surprising given the greater driving force for oxidation in aluminium alloys compared with ferrous alloys. While the driving force for oxidation is greater for aluminium than for steels, aluminium alloys exhibit substantially lower oxide growth rates compared with steels, a result of the fundamental difference in oxygen transport through the scale. Thus, in low temperature static oxidation of aluminium, a thin, stable oxide film is formed. However, in sliding contact, the oxide scale is continuously disrupted by the wear process greatly changing oxidation kinetics, shown for example by the observation that tribological values of the Arrhenius constant, Ap, are several orders of magnitude greater than the equivalents for static oxidation[17]. Therefore, it cannot be assumed that the generation of a stable ultra-thin oxide

layer that is found in low temperature static oxidation of Al will be found during the wear of aluminium.

The current results show that oxides do form at the worn surface of aluminium alloys, but they are often only observed when detailed surface examination is undertaken by TEM. For example, Fig. 12 shows a-Al2O3 at the surface of Duralcan. The oxide shows important differences with those formed on the ferrous materials. Firstly, there was always substantial cracking associated with the interface between a-Al2O3 and a-Al, in contrast to the ferrous alloys, where the interface was always free from cracking. While such cracking could have originated during TEM sample preparation, it is notable that no such cracking has ever been observed in mechanically alloyed Al alloys containing a-Al2O3,prepared in an identical fashion on an identical machine. Secondly, the a-Al2O3 was present as discrete, random shaped particles, which had not plastically deformed. In contrast, there was evidence that the ferrous oxides underwent plastic deformation for all materials studied here. Thus, as expected, there is clear evidence that thea-Al2O3 was substantially more brittle than the nonequilibrium oxide on the 316L or the Fe2O3/Fe3O4 formed on the tool steel and white irons.

The analysis of Quinn [10] showed that for ferrous alloys, the critical thickness at which the oxide spalled, ζ, was essentially constant as a function of load, although some small speed dependency was observed. Interestingly, x was also remarkably similar for Fe2O3,Fe3O4 and FeO, despite major differences in the asperity contact temperature, To. Unfortunately, values are not available for aluminium oxides, although the present work suggests that values of x appropriate to α-Al2O3are 50–150 nm (e.g. from Fig. 12) compared to the 1–3 μm reported by Quinn for ferrous oxides [10]. Thus, the oxide on the surface of the aluminium is removed before it is thick enough to be visible by SEM.

The reasons why oxides do not appear to be beneficial for Al alloys, but are for ferrous alloys, can be summarised as follows. Firstly, and most importantly, the critical thickness at which the oxide is detached as wear debris is approximately an order of magnitude smaller for aluminium compared to ferrous alloys. Secondly, and intimately related to the first reason, the ferrous oxides appear to be relatively ductile while the α-Al2O3 shows no evidence of ductility. Thirdly, the interface between the ferrous oxide and metal substrate appears to be strong, irrespective of the alloy composition, even where the oxide had become detached and then mechanically mixed into the surface. In contrast, under repeated asperity contact conditions, there was no evidence that the α-Al2O3 exhibited good adhesion with the substrate (TEM images always showed cracking at the interface between a-Al and a-Al2O3). Thus, the TEM evidence was that the ferrous oxides and oxygen-containing phases improved the mechanical properties of the surface. In contrast, there was no evidence that oxide at the surface of the a-Al improved mechanical properties, rather that the oxide/matrix interface acted as a potential site for crack nucleation.

No α-Al2O3 was found at the surface of the Al-based composite reinforced with Ni3Al particulate. Unlike the Duralcan material, there was extensive transfer of Fe from the counterface to the Al composite. In combination with the deformation and fragmentation of the

Ni3Al, a complex mechanically mixed layer was formed at the surface. In a similar manner to the ferrous tests, this MML exhibited good mechanical integrity and enhanced wear resistance.

The structure of the MML was extremely complex, and showed many similarities to the MML reported by Li and Tandon [65,66] for the sliding of Al–Si against an M2 tool steel. As with the current results, Li and Tandon could totally resolve the structure of the MML by conventional TEM. While electron spectroscopic imaging (ESI) has been available as a technique for a number of years, it has not been widely applied to the study of worn surfaces. The present results in Fig. 15show that mixing of the constituents occurs on a truly nm scale. It also demonstrates that oxidation is an important component of the MML, with the formation of a non-equilibrium amorphous Fe–Al–O phase. Moreover ,it is interesting that the Ni3Al exhibited signs of incorporating Fe into its structure, but showed no evidence of oxidation.

There are interesting parallels between the success of the oxide in enhancing wear resistance for the 316L and the MML in enhancing wear resistance for the Al–alloy/Ni3Al composite. In both cases, the various phases present (hard and soft) were plastically deformed to high strain and consequently became intimately mixed on a nm scale. In both cases, the deformation of a variety of different phases did not result in cracking, rather in the formation of ultra-fine scale composite. It is clear, therefore, that whether or not a reaction with the environment has a beneficial or detrimental effect on the wear rate depends strongly on the mechanical interaction of there action product with the substrate, particularly under conditions of surface plasticity.

4.5. Oxides of the surface of the hard coatings

Analysis of the wear regime under which the superhard TiAlN/CrN layer operated was difficult, since the wear rates were so low that no wear debris from the coating could be collected. The surface was smooth and exhibited the features frequently described as mild wear. However, SEM failed to reveal any oxide on the surface. In contrast, cross-sectional TEM demonstrated that the coating was covered in a uniform oxide film, containing an appreciable quantity of iron oxide (Fe3O4), but also a fraction of Al2TiO5, a product of oxidation of the coating itself. Thus, the wear could reasonably be described as mild oxidational. However, the surface film exhibited similarities, at least in some respects, to the surface of the Al–alloy/Ni3Al composite since it contained constituents from both surfaces. Thus, while the film was relatively uniform at contacting asperities, it did not comply with the sequence of events described by Quinn where the oxide film was formed by oxidation of one constituent.

Despite the differences described above, the surface oxide film exhibited the positive attributes of the oxide films found, for example, on the surface of the steels, namely, an ultra-fine structure with evidence of good adhesion with the substrate. Unfortunately, no comment can be made as to whether the film was beneficial or not, since the change in film thickness with load could not be measured and therefore a correlation of oxide surface coverage with wear rate could not be made.

5. Summary

(a) The oxide formed at the worn surface of the type 316L stainless steel comprised a non-equilibrium, oxygen-containing bcc nanocrystalline phase and anamorphous phase, both of which retained the same ratio of Fe:Cr as in the starting structure. The oxide had been deformed with the substrate, forming a nanoscale composite. The wear resistance of this composite structure exceeded that of the starting substrate.

(b) The oxide formed at the worn surface of the H21+7%TiC was predominantly Fe3O4, with a nanocrystalline structure, which became mechanically mixed with the substrate in a similar manner to the316L, although to a lesser extent. An increase in oxide coverage resulted in a reduction in wear coefficient.

(c) The oxide formed at the surface of the 17%Cr Fe was a thick (10 μm) uniform layer, consisting ofFe2O3 and Fe3O4. The grain size of the oxide was at least an order of magnitude larger than found for the H21+7%TiC or 316L, and there was little evidence of mechanical mixing with the substrate.

(d) The common observation with all ferrous oxides was the excellent adhesion between oxide and substrate, the absence of cracking within the oxide or at the substrate/oxide interface, and the apparently good ductility of the oxides.

(e) a-Al2O3 was observed at the surface of the Al–Si/30%SiC Dural can material. However, the oxide could only be detected in the TEM because of its fine dimensions (150 nm). Extensive cracking was present, particularly at the oxide/substrate interface. The absence of a beneficial effect was believed to be associated with the brittle nature of the oxide, its poor adhesion to the substrate under wear conditions, and the inability to generate a thick, stable oxide film.

(f) The Al–alloy Ni3Al composite exhibited a mechanically mixed layer at the surface, comprising constituents resulting from transfer of Fe from the counterface. An increase in the extent of the mechanically mixed layer resulted in a decrease in wear coefficient. The phases present had been extensively plastically deformed and selectively oxidised, resulting in a nanoscale composite, largely free from cracking, therefore exhibiting several similarities to the surface structure of the worn 316L.

(g) The worn surface of the TiAlN/CrN contained a thin(30 nm) film of oxide, comprising nanocrystallineFe3O4 (the Fe coming from the counterface) and Al2TiO5, not resolvable in the SEM. Thus, the wear of this coating could be described as mild oxidational.

References

[1] Fink M. Title. Trans Amer Soc Steel Treating 1026;1930:18.
[2] Quinn TFJ. Br J Appl Phys 1962;13:33.
[3] Quinn TFJ. ASLE Trans 1967;10:158.
[4] Quinn TFJ. Proc Inst Mech Eng 1968–69;183:pt3P,129.
[5] Quinn TFJ. Proc Inst Mech Eng 1967–68;182:3N.
[6] Quinn TFJ, Woolley JL. Lubr Eng, 1971;27,314.
[7] Quinn TFJ. ASLE Trans 1978;21:78.

[8] Sullivan JL, Quinn TFJ, Rowson DM. Tribol Int 1980;12:153.

[9] Rowson DM, Quinn TFJ. J Phys D 1980;13:208.

[10] Quinn TFJ. Tribology Int 1983;16:257.

[11] Quinn TFJ. Tribology Int 1983;16:305.

[12] Quinn TFJ, Winer WO. Wear 1985;102:67.

[13] Allen CB, Quinn TFJ, Sullivan JL. J Tribol 1986;32:1420.

[14] Hong H, Hochman RF, Quinn TFJ. Tribology Trans 1988;31:71.

[15] Quinn TFJ. Wear 1992;153:179.

[16] Quinn TFJ. Wear 1994;175:199.

[17] Quinn TFJ. Wear 1996;199:169.

[18] Sullivan JL, Hodgwon SG. Wear 1988;121:95.

[19] So H. Wear 1995;184:161.

[20] Rapoport L. Wear 1995;181–183:280.

[21] Vardavoulias M. Wear 1994;173:105.

[22] Li CS, Xu JZ, He XM, Liu XH, Wang CD. Mater Sci Technol 2000;16:501.

[23] Welsh NC. Phil Trans Roy Soc Series A 1965;257:31.

[24] Lim SC, Ashby MF. Acta Mater 1987;35:1.

[25] Rainforth WM, Stevens R, Nutting J. Phil Mag 1992;66:621.

[26] Perrin C, Rainforth WM. Wear 1995;181–183:312.

[27] Perrin C, Rainforth WM. Wear 1997;203–204:171.

[28] Leonard AJ, Perrin C, Rainforth WM. Mater Sci 62 Trans 1997;13:41.

[29] Hanlon DN, Rainforth WM, Sellars CM. Wear 1997;203–204:220.

[30] Perrin C, Rainforth WM. Scripta Mater 1996;34:877.

[31] Rainforth WM, Leonard AJ, Perrin C, Jang SK. Proceedings of the 28th Leeds Lyon Conference, Elsevier, 2001, in press.

[32] Luo Q, Mu¨nz D-W, Rainforth WM. Wear 1999;225–229:74.

[33] Luo Q, Mu¨nz D-W, Rainforth WM. Scripta Mater 2001;45:399.

[34] Luo Q, Mu¨nz D-W, Rainforth WM. Surface Coat Technol 2001;146–147:430.

[35] Wang Y, Rainforth WM, Jones H, Lieblich M. Wear 2001;250:1421.

[36] Bedolla Jacuinde A, Rainforth WM. Wear 2001;250:449.

[37] Torres B, Wang Y, Lieblich M, Ibanez J, Rainforth WM, Jones H. Z. Metallkunde 2001;92:604.

[38] Manning MJ, Rowlands PC. British Corrosion Journal 1980;15:428.

[39] Newcomb S, Stobbs W. Mater Sci & Eng 1984;66:195.

[40] Hofer F, Warbichler P, Grogger W. Ultramicroscopy 1995;59:15.

[41] Warbichler P, Hofer F, Hofer P, Letofsky E. Micron 1998;29:63.

[42] Hofer F, Warbichler P, Buchmayr B, Kleber S. J Microsc 1996;184:163.

[43] Moore MA, Douthwaite RM. Met Trans 1976;7A:1833.

[44] Saito N, Hemmi Y, Arima T, Oishi M, Hosokawa M. Wear 1996;201:145.

[45] Antoniou R, Subramanian C. Scripta Mater 1988;22:809.

[46] Smith AF. Wear 1986;110:151.

[47] Smith AF. Wear 1985;105:91.
[48] Smith AF. Tribology Interntl 1985;18:35.
[49] Smith AF. Tribology Interntl 1986;19:65.
[50] Suryanarayana C. Progress in Materials Science, 2001;46:1.
[51] De-Wit E, Froyen L, Celis J-P. Wear 1999;231:116.
[52] Li XY, Tandon KN. Scripta Mater 1995;33:485.
[53] Wang Y, Gao CQ, Lei TC, Lu HX. Scripta Mater 1988;22:251.
[54] Van Herpen A, Reynier B, Phalippou C. Wear 2001;249:37.
[55] Yang ZY, Naylor MGS, Rigney DA. Wear 1985;105:73.
[56] Cook DC. Metall Trans 1987;18A:201.
[57] Lancaster JK. Wear 1967;10:103.
[58] Venkataraman B, Sundararajan G. Acta Mater 1996;44:451.
[59] Venkataraman B, Sundararajan G. Acta Mater 1996;44:461.
[60] Barlow IC, Rainforth WM, Jones H. Acta Mater 2001;49:1209.
[61] Wood PD, Datta PK, Burnell-Gray JS, Wood N. Mater Sci Forum 1997;251–254:467.
[62] Stott FH, Wood GC. Tribol Int 1978;11:211.
[63] Jiaren J, Stott FH, Stack MM. Wear 1994;176:185.
[64] Berns H, Koch S. Wear 1999;225–229:154.
[65] Li XY, Tandon KN. Wear 1999;225–229:640.
[66] Li XY, Tandon KN. Wear 2000;245:148.